Clean Energy, 2020, Vol. 4, No. 4, 328–348

doi: 10.1093/ce/zkaa019
Advance Access Publication Date: 22 December 2020
Homepage: https://academic.oup.com/ce

Research Article

Integration of solid-oxide fuel cells and absorption refrigeration for efficient combined cooling, heat and power production

Krzysztof Matuszny[1], Tohid N. Borhani[2], Seyed A. Nabavi[1] and Dawid P. Hanak[1,*]

[1]Energy and Power, School of Water, Energy and Environment, Cranfield University, Bedford, Bedfordshire, MK43 0AL, UK
[2]School of Engineering and Physical Sciences, Heriot-Watt University, Edinburgh, EH14 4AS, UK

*Corresponding author. E-mail: d.p.hanak@cranfield.ac.uk

Abstract

Combined cooling, heating and power (CCHP) systems are characterized by a substantially higher energy-utilization efficiency compared to standalone systems. In this study, an integrated system comprising a solid-oxide fuel cell (SOFC), hot-water storage tank (HWST) and absorption refrigeration (AR) cycle is considered. The SOFC model was developed in Aspen Plus®. It was used to determine the thermodynamic properties of the exhaust gas that was then used to provide heat for the HWST and to drive the AR cycle. Thermodynamic models for the AR cycles were developed in Engineering Equation Solver, considering LiBr–H_2O and NH_3–H_2O as working fluids. The sensitivity analysis of a number of SOFC output parameters has been carried out. The most optimal case was characterized with the coefficient of performance (COP) and CCHP efficiency of 0.806 and 85.2% for the LiBr–H_2O system, and 0.649 and 83.6% for the NH_3–H_2O system, respectively. Under such optimal operating conditions, the SOFC was characterized by the net electrical efficiency of 57.5% and the net power output of 123.66 kW. Data from the optimal solution were used to perform the thermodynamic study and sensitivity analysis to assess the influence of different absorption cycle operating conditions and to identify possible applications for the considered integrated systems.

Received: 22 July 2020; **Accepted:** 14 September 2020

Graphical Abstract

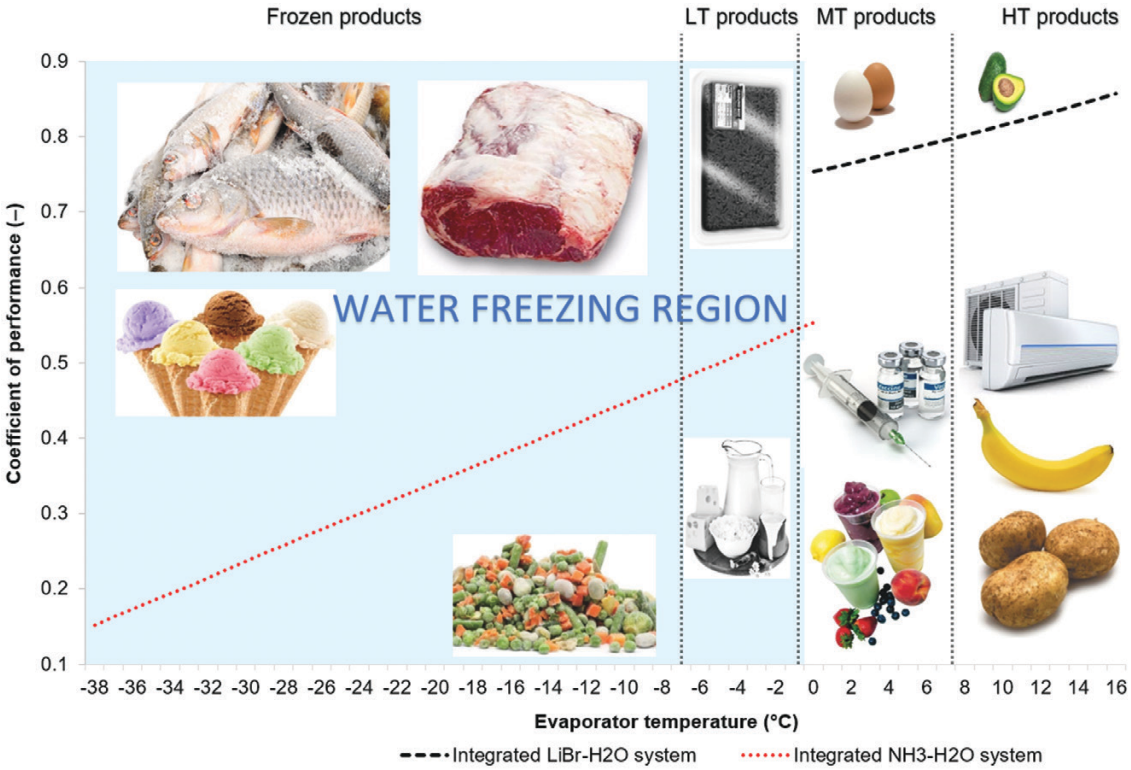

Keywords: solid-oxide fuel cell; absorption refrigeration; hot-water storage tank; process integration; tri-generation

Introduction

With the rising global mean temperature, which is primarily caused by global warming, the heating and cooling profile is forecasted to change. The demand for cooling is expected to approximately be the same as that for heating by 2030 [1]. For this reason, innovative concepts that combine the production of cooling, heating and power from one energy source, which are known as tri-generation or combined cooling, heating and power (CCHP) plants, are being developed [2]. Compared to standalone generation systems, a tri-generation system is characterized primarily by a higher total efficiency, reduced fuel and energy costs, and lower greenhouse-gas emissions. A tri-generation system generally includes the prime mover, the heat-recovery system, the cold-production system, and the management and control system.

The most common prime movers utilized in tri-generation systems are gas or steam turbines, internal-combustion or Stirling engines and high-temperature fuel cells, such as a solid-oxide fuel cell (SOFC) [3, 4]. A micro-gas turbine (MGT) is considered as one of the best existing primary movers for application in combined systems [5]. Vera et al. [6] considered an MGT integrated with an organic Rankine cycle (ORC) for combined heat and power generation based on biomass gasification. This system was then used as a basis for the development of a tri-generation system, which included an NH_3–H_2O adsorption chiller, by El-Sattar et al. [7, 8]. Although the overall efficiency of the CCHP system was reported to be 42–47%, the net electrical efficiency was only 20–22% with the ORC. The study by Ozcan and Dincer [9] showed that using the SOFC as the prime mover can increase the net electrical efficiency of the tri-generation system based on biomass gasification to 36.5% while achieving high CCHP efficiency (42.2%). The SOFC is a high-temperature fuel cell that typically operates at 600–1000°C and converts the chemical energy of a fuel, such as carbon monoxide, methane or other hydrocarbons and energy vectors, such as hydrogen, into electrical energy [10]. The main advantages of the SOFC over other prime movers are its high electrical efficiency (50–60%) and the high temperature of the exhaust gas that can be further used for heating purposes or/and cooling purposes by passing hot gases via an absorption refrigeration (AR) cycle. Despite these advantages, the current literature indicates that such tri-generation systems have not been thoroughly evaluated. Sulaiman et al. [11] examined the thermodynamic performance of the integration of the SOFC fuelled by methane and the ORC system for cooling, heating and power production. Their work has shown that the tri-generation system can result in a 3–25% point increase in exergy efficiency compared to the standalone power-cycle system. Yu et al.

[12] presented a tri-generation system based on the SOFC fuelled by natural gas and a double-effect LiBr–H_2O absorption chiller. The system can achieve a total efficiency of at least 84%. Zhao et al. [13] proposed an integrated SOFC–CCHP system that was fuelled by coke oven gas containing a large amount of hydrogen. The SOFC operated at 6–13 bar and was integrated with a gas turbine. The flue gas at the exit of the heat-recovery steam generator, which produced steam for a steam Rankine cycle, was used for district heating. The latent heat of the steam leaving the steam turbine was used for cooling in a single-effect LiBr–H_2O absorption chiller. Such a tri-generation system was characterized by the electrical efficiency of the SOFC of >60%. The total electrical efficiency and the total efficiency of the SOFC–CCHP system were about 70% and 90%, respectively. Venkataraman et al. [14] proposed a system that integrates the SOFC fuelled by hydrogen and the NH_3–H_2O system in a truck to produce cooling for food refrigeration (transportation storage) and electricity to power truck auxiliary devices. The excess electricity was assumed to charge the truck's battery. The considered systems were coupled with thermal oil and a gas–oil heat exchanger in which the oil was heated to the temperature required by the desorber. That study demonstrated that the SOFC with a power output of <10 kW was sufficient to provide cooling for small (0.7-ton), medium (12-ton) and large (40-ton) trucks, considering a maximum temperature inside the refrigeration cabinet of –20°C. Elmer et al. [15] experimentally investigated a tri-generation system based on the SOFC fuelled by natural gas, LiBr–H_2O system and hot-water cylinder. The SOFC was connected to the natural-gas grid and to the electricity grid to export electricity. The exhaust gas from the SOFC supplied heat to the AR system via a liquid-desiccant system feeding hot flue gases to a hot-water cylinder. Due to the technical issue with the SOFC, the study was performed using empirical data for the SOFC and liquid-desiccant systems. Nevertheless, the study demonstrated that the integration of a 1.5- and a 2-kW SOFC with AR and a hot-water cylinder resulted in a total efficiency of the tri-generation system of 68.9 and 71.1%, respectively. The economic assessment of such a system, however, indicated that it was only feasible if additional incentives, such as feed-in tariffs, were considered. This was mainly due to a high capital cost of the SOFC and the necessity for replacing the fuel-cell stack every 5 years. Hou et al. [16] presented a distributed energy system based on a solar methanol-reforming SOFC that combined gas turbine–steam turbine (GT–ST) power-generation system with absorption heat pump–absorption regeneration (AHP–AR). The results showed that the efficiency of the SOFC, total electrical efficiency and total efficiency were 35%, 66% and 90%, respectively.

The AR systems that are mostly considered for integration with the SOFC are based on NH_3–H_2O and LiBr–H_2O working fluids. However, the SOFC–CCHP systems considering these AR systems have not been directly compared in the current literature. Therefore, this study aims to compare the performance of the SOFC–CCHP systems based on the NH_3–H_2O and LiBr–H_2O working fluids and to determine the optimum application. To achieve this, the SOFC is integrated with a hot-water storage tank (HWST) and AR system using a different pair of working fluids. The optimal output parameters of the SOFC, which was modelled in Aspen Plus®, for AR systems are determined. The thermodynamic assessment is then performed using Engineering Equation Solver (EES) to evaluate the performance of the LiBr–H_2O and NH_3–H_2O absorption cycles under different operating conditions. Finally, the sensitivity analysis is performed to evaluate the effect of the key parameters of AR on the tri-generation system performance. The LiBr–H_2O and NH_3–H_2O systems are compared and analysed.

1 Model development and validation

1.1 The SOFC model

A SOFC model used in this study was developed by Hanak et al. [17] based on the work presented by Zhang et al. [18]. This model has been revised to incorporate the electrochemical model of Doherty et al. [19] and enables the utilization of different fuels. The thermodynamic model has been described in detail by Hanak et al. [17]. The schematic diagram of the SOFC is shown in **Fig. 1**.

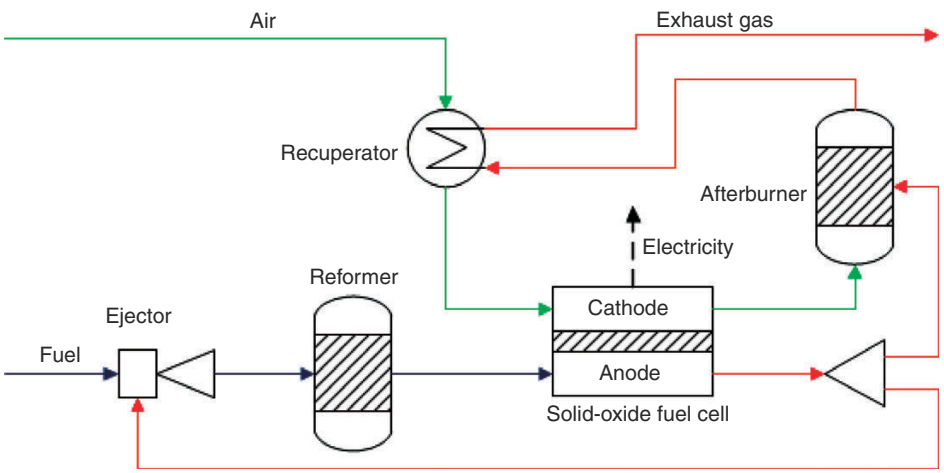

Fig. 1: Schematic diagram of a solid-oxide fuel cell

The considered electrochemical model utilizes the Nernst equation, which is defined in Equation (1) to determine the reversible Nernst voltage. Furthermore, to account for the irreversibilities in the SOFC, the Ohmic (V_{Ohmic}) [20], activation ($V_{Activation}$) [21] and concentration ($V_{Activation}$) [22] losses are determined in Equations (1)–(4), respectively. Finally, Equation (5) is used to estimate the actual voltage (V) of the SOFC.

$$V_{Nernst} = -\frac{\Delta \bar{g}_f}{2 \cdot F} + \frac{R_g \cdot T_{avg}}{2 \cdot F} \ln\left(\frac{P_{H_2} \cdot P_{O_2}^{0.5}}{P_{H_2O}}\right) \quad (1)$$

$$V_{Ohmic} = \underbrace{\frac{j \cdot \rho_A (A \cdot \pi \cdot D_m)^2}{8 \cdot t_A}}_{\text{Anode}} + \underbrace{\frac{j \cdot \rho_A (A \cdot D_m)^2}{8 \cdot t_A} \cdot A\,(A + 2\,(1 - A - B))}_{\text{Cathode}} + \underbrace{j \cdot \rho_E \cdot t_E}_{\text{Electrolyte}} + \underbrace{j \cdot \rho_I \cdot \pi \cdot D_m \frac{t_I}{w_I}}_{\text{Interconnection}} \quad (2)$$

$$V_{Activation} = \underbrace{\frac{2 \cdot F}{R_g \cdot T_{SOFC}} k_A \left(\frac{P_{H_2}}{P_0}\right)^m \exp\left(\frac{-E_A}{R_g \cdot T_{SOFC}}\right)}_{\text{Anode}} + \underbrace{\frac{4 \cdot F}{R_g \cdot T_{SOFC}} k_C \left(\frac{P_{O_2}}{P_0}\right)^m \exp\left(\frac{-E_C}{R_g \cdot T_{SOFC}}\right)}_{\text{Cathode}} \quad (3)$$

$$V_{Concentration} = \underbrace{\left(\frac{-R_g \cdot T_{SOFC}}{2 \cdot F}\right) \ln\left(\frac{1 - \left(\frac{R_g \cdot T_{SOFC}}{2 \cdot F}\right)\left(\frac{t_A}{D_A^{eff} \cdot y^0_{H_2} \cdot P_{SOFC}}\right)_j}{1 + \left(\frac{R_g \cdot T_{SOFC}}{2 \cdot F}\right)\left(\frac{t_A}{D_A^{eff} \cdot y^0_{H_2O} \cdot P_{SOFC}}\right)_j}\right)}_{\text{Anode}} + \underbrace{\left(\frac{-R_g \cdot T_{SOFC}}{4 \cdot F}\right) \ln\left(\frac{\frac{P_{SOFC}}{\delta_{O_2}} - \left(\frac{P_{SOFC}}{\delta_{O_2}} - y^0_{O_2} \cdot P_{SOFC}\right) \exp\left(\frac{R_g \cdot T_{SOFC}}{4 \cdot F}\left(\frac{\delta_{O_2} \cdot t_C}{D_C^{eff} \cdot y^0_{H_2} \cdot P_{SOFC}}\right)_j\right)}{y^0_{O_2} \cdot P_{SOFC}}\right)}_{\text{Cathode}} \quad (4)$$

$$V = V_{Nernst} - (V_{Ohmic} + V_{Activation} + V_{Concentration}) \quad (5)$$

In Equations (1)–(4), $\Delta \bar{g}_f$ is the molar Gibbs free energy of formation at 1 bar (J/mol); T_{avg} and T_{SOFC} are the averages of the temperatures between the SOFC inlet and outlet streams and the SOFC operating temperature, respectively (K); F is the Faraday constant (96 485 C/mol); R_g is the molar gas constant (8.314 J/mol K); P_i is the partial pressure (bar) of gaseous component i; P_0 is the reference pressure (1 bar); ρ_i is the resistivity term (Ωm) that is a function of temperature [23]; D_m is the mean diameter of a cell (m); t_i is the cell component thickness (m); k_A and k_C are pre-exponential factors (A/m^2) and are 2.13 × 10^8 and 1.49 × 10^{10}, respectively; m is the slope and is equal to 0.25; E_A and E_C are activation energy (J/mol) with values of 110 000 and 160 000, respectively; P_{SOFC} is the SOFC operating pressure (Pa); D_i^{eff} is the effective diffusion coefficient (m^2/s); y_i^0 is the mole fraction of gaseous component i in bulk flow; j is the current density (A/m^2). A, B and δ_{O_2} are constants [19]; and w_I is the interconnection width (0.009 m). The SOFC model has been validated with the data presented by Veyo et al. [24–26], Zhang et al. [19] and Doherty et al. [18] (see the online Supplementary Data). The input data for the SOFC model used in this study are presented in Table 1.

1.2 The AR model

Thermodynamic models for AR cycles have been developed using EES, as it comprises built-in external libraries for LiBr–H_2O and NH_3–H_2O. In each of the considered AR systems, the HWST has been implemented for waste-heat utilization. The AR models have been developed considering the following assumptions [27, 28]:

- the system is in steady state;
- temperature variations in the evaporator, condenser, absorbent and generator are negligible;
- the throttling devices are adiabatic;
- the pressure drop and heat loss to the environment in all components and connecting pipes and fittings are negligible;
- the refrigerant leaving the condenser and the evaporator is considered to be saturated liquid and saturated vapour, respectively;
- the temperature difference between the outlet and inlet of heat-rejection devices is 5°C (for both absorber and condenser);
- the temperature approach between the outlets of the heating circuit and the generator solution/refrigerant is 10°C;
- the temperature approach between the evaporator inlet and cooling air supply (to the cooling application) is 5°C;
- the temperature decrease through the condenser is assumed to equal to 4°C (for NH_3–H_2O);
- the equilibrium at high and low pressure corresponds to the temperature and mass fraction of the NH_3–H_2O solution in the condenser and evaporator, respectively (for NH_3–H_2O);

Table 1: Input data for the SOFC simulation in Aspen[18, 19] Plus®

Parameter	Value
Fuel-inlet composition (%$_{vol}$)	
CH_4	81.3
C_2H_6	2.9
C_3H_8	0.4
C_4H_{10}	0.2
N_2	14.3
CO	0.9
Fuel flow rate (kg/s)	0.0056
Lower heating value of natural gas (MJ/kg)	38.45
Cell operating pressure (bar)	1.08
Power output (kW, DC)	120
Active area (m^2)	96.1
Cell-exhausts temperature (°C)	910
Inlet air temperature (°C)	630
Inlet fuel temperature (°C)	200
DC-to-AC inverter efficiency (–)	0.92
Overall fuel-utilization factor (–)	0.85
S/C ratio (–)	2.5
Temperature difference between the outlet of the cold and hot streams in the recuperator (°C)	10
SOFC thermal losses (%)	2

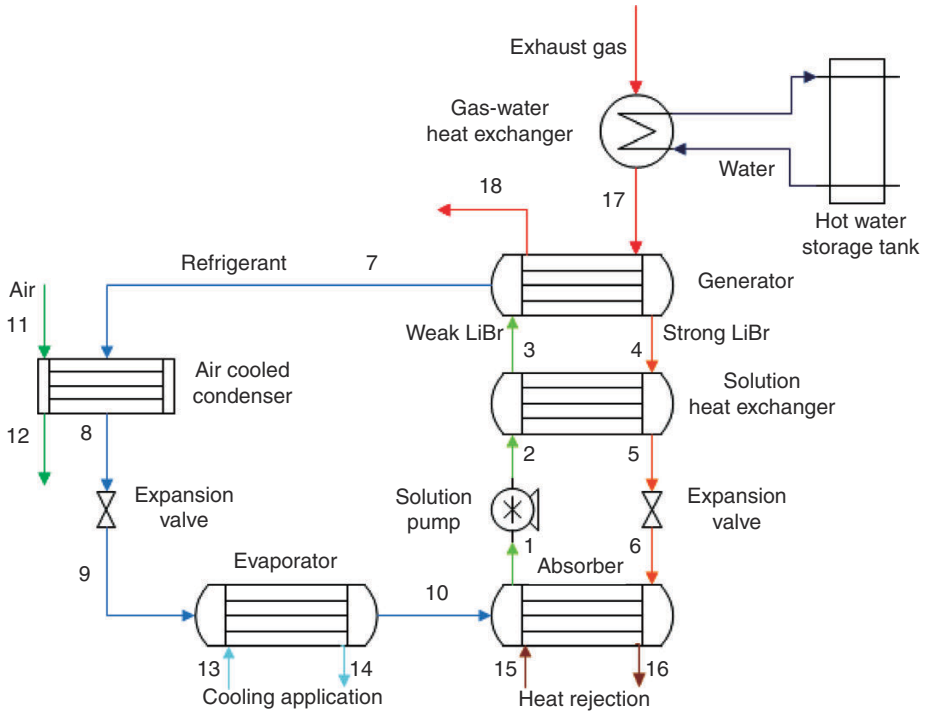

Fig. 2: Schematic diagram of the LiBr–H_2O system

- negligible difference between the molar and mass fraction of the ammonia–water mixture (for NH_3–H_2O); and
- the vapour quality of the evaporator outlet (state 13) is 0.975 (for NH_3–H_2O).

1.2.1 *The LiBr–H_2O system*

A single-effect LiBr–H_2O system, the thermodynamic model for which has been developed in EES, is presented in Fig. 2. The AR system is integrated with the SOFC. Since exhaust gas leaves the SOFC at a high temperature (>180°C), which depends on the operating conditions of the SOFC, it is necessary to reduce its temperature to meet the temperature requirements of the generator in the LiBr–H_2O system. This is achieved in the gas–water heat exchanger (GWHX) where heat from the exhaust gas is used to heat up the water in a storage tank. The exhaust gas leaves GWHX at state 17 and transfers its remaining thermal energy to the generator at the required temperature. It is then released into the environment at state 18. Heat is removed from the condenser and the absorber using ambient air, which enters the condenser and the absorber at states 11 and 15, respectively. The cooling effect is produced in the evaporator and is used to cool the return air at state 13. The resulting colder air is supplied to the cooling or refrigeration application at state 14.

The input parameters to the LiBr–H_2O model, the thermodynamic equations and constraints for which are presented in Table 2, are:

- mass flow rate and temperature of flue gases leaving the SOFC;
- supply and return temperature of the HWST ($water_{in}$, $water_{out}$);
- the temperature of components in the internal loop, including absorber (state 1), condenser (state 8) and evaporator (state 10);
- inlet temperatures of the external coils, including the condenser (state 11) and absorber (state 15), which are equal to the assumed ambient air temperature;
- the temperature approach for the generator (between states 18 and 4) and evaporator (states 14 and 10);
- the temperature difference between the inlet and outlet of the absorber (states 15 and 16) and condenser (states 11 and 12);
- pump efficiency; and
- the effectiveness of the heat exchangers.

1.2.2 *The NH_3–H_2O system*

Fig. 3 shows the integration of the NH_3–H_2O system with the SOFC. As in the case of the LiBr–H_2O system, the temperature of the SOFC exhaust gas has been reduced in the GWHX to meet the requirement of the generator. The exhaust gas leaves the GWHX at state 14 and transfers its remaining thermal energy to the generator at the required temperature. It is then released into the environment at state 15. Heat is removed from the condenser and the absorber using ambient air, which enters the condenser and the absorber at states 16 and 20, respectively. The cooling effect is produced in the evaporator and is used to cool the return air at state 18. The resulting colder air is supplied to the cooling or refrigeration application at state 19. In contrast to the LiBr–H_2O system, the NH_3–H_2O system needs a rectifier as the superheated vapour leaving the generator at state 8 comprises water droplets that need to be removed before entering the condenser at state 10.

Table 2: Equations and constraints for the LiBr–H_2O model

Model equations	
High-side pressure	$p_{high} = p_{sat}(t_8) = p_2 = p_3 = p_4 = p_5 = p_7 = p_8$
Low-side pressure	$p_{low} = p_{sat}(t_{10}) = p_1 = p_6 = p_9 = p_{10}$
Enthalpy at the condenser outlet	$h_8 = h_{water}(t_8, p_8)$
Enthalpy at the evaporator outlet	$h_{10} = h_{steam_{IAPWS}}(t_{10}, p_{10})$
Enthalpy at the generator outlet	$h_7 = h_{steam\_IAPWS}(t_7, p_7)$
Effectiveness of GWHX	$\varepsilon_{GWHX} = \frac{t_{SOFC} - t_{17}}{t_{SOFC} - t_{water,out}}$
Heat-transfer rate of SOFC (equal to that of HWST)	$\dot{Q}_{SOFC} = \dot{m}_{SOFC} \cdot cp_{SOFC} \cdot (t_{SOFC} - t_{17}) = \dot{Q}_{tank}$
Effectiveness of the generator heat exchanger	$\varepsilon_{GHX} = \frac{t_{17} - t_{18}}{t_{17} - t_7}$
Temperature approach between flue gas outlet and generator outlet	$\Delta T_{app,g} = t_{18} - t_4$
Heat supplied to generator component	$\dot{Q}_g = \dot{m}_{SOFC} \cdot cp_{SOFC} \cdot (t_{17} - t_{18}) = \dot{m}_7 \cdot h_7 + \dot{m}_4 \cdot h_4 - \dot{m}_3 \cdot h_3$
Weak and strong concentration of LiBr–H_2O	$X_{weak} = X_{LiBrH_2O}(t_1, p_1) = X_1 = X_2 = X_3$ $X_{strong} = X_{LiBrH_2O}(t_4, p_4) = X_4 = X_5 = X_6$
Enthalpy at state 4	$h_4 = h_{LiBrH_2O}(t_4, X_4)$
Mass flow rate of the strong solution	$\dot{m}_1 \cdot X_1 = \dot{m}_6 \cdot X_6,\ \dot{m}_1 = \dot{m}_2 = \dot{m}_3,\ \dot{m}_6 = \dot{m}_5 = \dot{m}_4$
Refrigerant mass flow rate	$\dot{m}_7 = \dot{m}_3 - \dot{m}_4,\ \dot{m}_7 = \dot{m}_8 = \dot{m}_9 = \dot{m}_{10}$
Heat capacities of the strong- and weak-solution streams	$\dot{C}_2 = \dot{m}_2 \cdot cp_2$ and $\dot{C}_4 = \dot{m}_4 \cdot cp_4$
Specific heat for each stream	cp_2 and cp_4 are determined by external EES routine for LiBr–H_2O
Maximum heat-transfer rate	$\dot{Q}_{max} = \dot{C}_{min} \cdot (t_4 - t_2),\ \dot{C}_{min} = \min\{\dot{C}_2, \dot{C}_4\}$
Actual heat-transfer rate	$\dot{Q}_{actual} = \varepsilon_{SHX} \cdot \dot{Q}_{max}$
Outlet temperatures at states 3 and 5	$t_3 = t_2 + \frac{\dot{Q}_{actual}}{\dot{C}_2}$ and $t_5 = t_4 - \frac{\dot{Q}_{actual}}{\dot{C}_4}$
Enthalpy at states 3 and 5	$h_3 = h_{LiBrH_2O}(t_3, p_3)$ and $h_5 = h_{LiBrH_2O}(t_5, p_5)$
Enthalpy at states 6 and 9	$h_6 = h_5$ and $h_9 = h_8$
Enthalpy at state 2	$\dot{m}_2 \cdot h_2 + \dot{m}_4 \cdot h_4 - \dot{m}_3 \cdot h_3 - \dot{m}_5 \cdot h_5 = 0$
Heat-transfer rate at the absorber, condenser and evaporator	$\dot{Q}_a = \dot{m}_{10} \cdot h_{10} + \dot{m}_6 \cdot h_6 - \dot{m}_1 \cdot h_1$ $\dot{Q}_c = \dot{m}_7 \cdot (h_7 - h_8)$ $\dot{Q}_e = \dot{m}_9 \cdot (h_{10} - h_9)$
Required pump work within solution cycle	$\dot{W}_p = \frac{\dot{m}_1 \cdot (p_2 - p_1)}{\rho_1}$
Density at state 1	$\rho_1 = \rho_{LiBrH_2O}(t_1, p_1)$ ρ_1 is obtained from an external EES routine for LiBr–H_2O
Coefficient of performance (COP) of the system	$COP = \frac{\dot{Q}_e}{\dot{Q}_g + \dot{W}_p}$
Efficiency of combined cooling and power plant (CCP) and combined cooling, heating and power plant (CCHP)	$\eta_{CCP} = \frac{\dot{Q}_e + N_{el}}{\dot{m}_{fuel} \cdot LHV}$ and $\eta_{CCHP} = \frac{\dot{Q}_e + N_{el} + \dot{Q}_{tank}}{\dot{m}_{fuel} \cdot LHV}$
Model constraints	
Minimum allowable generator temperature	$tg_{min} = 2 \cdot t_c - t_e$
Critical LiBr–H_2O concentrations for the weak and strong solutions [29]	$X_{c1} = \frac{0.0809 * t_1 + 61.341}{100}$ $X_{c4} = \frac{0.0809 * t_4 + 61.341}{100}$

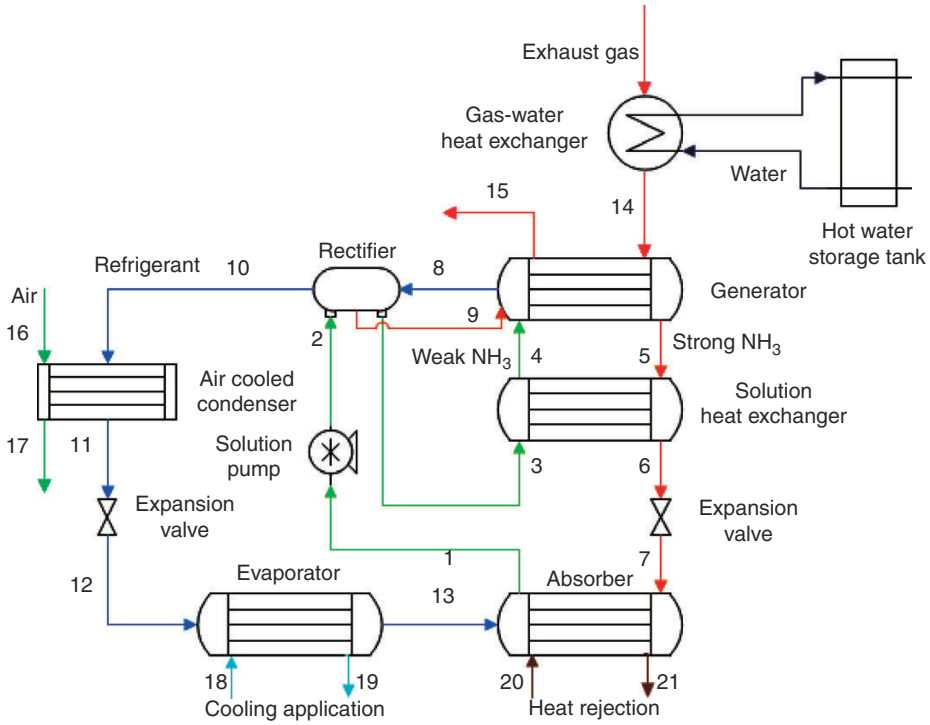

Fig. 3: Schematic diagram of the NH_3–H_2O system

The input parameters to the NH_3–H_2O model, the thermodynamic equations and constraints for which are presented in Table 3, are:

- mass flow rate and temperature of flue gases leaving the SOFC;
- supply and return temperature of the hot-water storage tank ($water_{in}$, $water_{out}$);
- the temperature of components in the internal loop, including the absorber (state 1), condenser (state 11) and evaporator (state 12);
- inlet temperatures of the external coils: condenser (state 16) and absorber (state 20), which are equal to the assumed ambient air temperature;
- the temperature approach for the generator (between states 18 and 7) and evaporator (states 14 and 10);
- the temperature difference between the inlet and outlet of the absorber (states 20 and 21) and condenser (states 16 and 17);
- pump efficiency; and
- the effectiveness of the heat exchangers.

1.2.3 *Validation of the AR models*

The thermodynamic models for the LiBr–H_2O and NH_3–H_2O systems were validated using the data presented in the literature. The LiBr–H_2O model was validated using data presented by Rubio-Maya [30] and the NH_3–H_2O model was validated using data presented by Keith et al. [31]. The input parameters used to validate the AR models are listed in Table 4. Validation of the AR models focused only on the internal loop of the AR cycles, as the reference data (temperature, pressure, flow rates) are independent of the external loop. The coefficient of performance (COP) was used as the key performance indicator to assess the performance of the AR system. As the comparison model did not consider the heat recovery from the rectifier, the heat-transfer rate in the rectifier was included in the COP calculations, as shown in Equation (6):

$$COP = \frac{\dot{Q}_e}{\dot{Q}_g + \dot{Q}_r + \dot{W}_p} \tag{6}$$

Table 5 reveals the performance prediction of the models developed in this work and its comparison with the reference data. Overall, the prediction of both AR models was found to be close to that reported in the literature. The prediction of the LiBr–H_2O model is consistent with that presented by Rubio-Maya et al. [30]. The difference in the COP and the generator heat-transfer rate resulted from the calculation method used in this work. Namely, this work assumed that the temperature of the vapour refrigerant was in equilibrium with the concentration of the weak LiBr solution. On the contrary, the reference model assumed that the generator-outlet temperatures of the weak LiBr solution and refrigerant were the same. Moreover, the difference in the pressure and LiBr concentration were due to different sources of thermodynamic properties used in this work and in the reference model.

The prediction of the NH_3–H_2O model developed in this work was observed to closely reflect the prediction of the model presented by Keith et al. [31]. The largest deviation was observed for the rectifier heat-transfer rate, which was <5% lower than that in the reference model. Similarly to the LiBr–H_2O system, this can be associated with different sources of thermodynamic properties used in this work and in the reference model.

Table 3: Equations and constraints for the NH_3–H_2O model

Model equations	
Heat applied to the generator from the external circuit	$\dot{Q}_g = \dot{m}_8 \cdot h_8 + \dot{m}_5 \cdot h_5 - \dot{m}_4 \cdot h_4$
Mass fraction of vapour at state 10	$y_{10} = y_{NH_3H_2O}(t_{10}, p_{10_{guess}}, Q_{10} = 1)$
High-side pressure at state 11 (calculations involve iterative technique)	$p_{11} = p_{NH_3H_2O}(t_{11}, x_{11}, Q_{11} = 0)$
Converged value of p_{11} fixes other high pressures inside a system	$p_{11} = p_2 = p_3 = p_4 = p_5 = p_6 = p_8 = p_9 = p_{10}$
Enthalpy of liquid solution at state 11	$h_{11} = h_{NH_3H_2O}(t_{11}, x_{11}, Q_{11} = 0)$
Mass fraction of liquid and vapour	$x_{12} = x_{NH_3H_2O}(t_{12}, p_{12}, Q_{12} = 0)$ $y_{12} = y_{NH_3H_2O}(t_{12}, p_{12}, Q_{12} = 1)$
Enthalpy of liquid and vapour solutions	$h_{12,l} = h_{NH_3H_2O}(t_{12}, x_{12}, Q_{12} = 0)$ $h_{12,v} = h_{NH_3H_2O}(t_{12}, y_{12}, Q_{12} = 1)$
Enthalpy before and after the expansion valve	$h_{11} = h_{12}$
Enthalpy equality between liquid and vapour solution	$f_l = \frac{h_{11} - h_{12,v}}{h_{12,l} - h_{12,v}}$
Actual mass fraction at state 12	$x_{12,actual} = 1 + \frac{x_{11} - 1}{f_l}$
Low-side pressure in the system (the new value of p_{12} is used in a repeat loop of calculations to find a new estimate for a mass fraction at state 12)	$p_{12} = p_{NH_3H_2O}(t_{12}, x_{12,actual}, Q_{12} = 0)$
Convergence criteria	$p_{12} = p_1 = p_7$
Mass fractions and enthalpy for the known outlet temperature of the absorber	$x_1 = x_{NH_3H_2O}(t_1, p_1, Q_1 = 0)$ $h_1 = h_{NH_3H_2O}(t_1, x_1, Q_1 = 0)$
Applying mass-fraction equilibrium for a rich solution ($x_1 = x_2 = x_3 = x_4$) as well as assuming that the mass fraction of a dripped solution is in equilibrium with an incoming rich solution ($x_9 = x_4$), the temperature and enthalpy at state 9	$t_9 = t_{NH_3H_2O}(p_9, x_9, Q_9 = 0)$ $h_9 = h_{NH_3H_2O}(t_9, x_9, Q_9 = 0)$
Since $t_9 = t_8$, the mass fraction of the vapour solution at state 8	$y_8 = y_{NH_3H_2O}(t_8, p_8, Q_8 = 1)$ $h_8 = h_{NH_3H_2O}(t_8, y_8, Q_8 = 1)$
Mass-fraction equality exists for a weak solution ($x_5 = x_6 = x_7$)	$x_5 = x_{NH_3H_2O}(t_5, p_5, Q_5 = 0)$ $h_5 = h_{NH_3H_2O}(t_5, x_5, Q_5 = 0)$
Converged mass fraction of liquid solution at state 12 is in equilibrium with the vapour solution leaving the evaporator ($x_{12} = y_{13}$). With that equality and assumption, that vapour quality at this state is 0.975	$t_{13} = t_{NH_3H_2O}(p_{13}, y_{13}, Q_{13} = 0.975)$ $h_{13} = h_{NH_3H_2O}(t_{13}, y_{13}, Q_{13} = 0.975$
Mass flow rates in a system (ω is the mass fraction of ammonia in liquid or vapour state)	$\sum_{in} \dot{m} = \sum_{out} \dot{m}$ and $\sum_{in} \dot{m} \cdot \omega = \sum_{out} \dot{m} \cdot \omega$
Mass flow-rates equality for rich, weak and refrigerant solutions	$\dot{m}_1 = \dot{m}_2 = \dot{m}_3 = \dot{m}_4$ $\dot{m}_5 = \dot{m}_6 = \dot{m}_7$ $\dot{m}_{10} = \dot{m}_{11} = \dot{m}_{12} = \dot{m}_{13}$
Relation governing the mass balance around the generator that links the heat input to the generator with mass fractions	$\dot{m}_4 \cdot x_4 + \dot{m}_9 \cdot x_9 = \dot{m}_8 \cdot y_8 + \dot{m}_5 \cdot x_5$

Table 3: Continued

Model equations	
Mass and energy balance for the rectifier	$\dot{m}_8 \cdot h_8 + \dot{m}_2 \cdot h_2 - \dot{m}_3 \cdot h_3 - \dot{m}_9 \cdot h_9 - \dot{m}_{10} \cdot h_{10} = 0$ $\dot{m}_8 = \dot{m}_{10} + \dot{m}_9$ $\dot{Q}_r = \dot{m}_8 \cdot h_8 - \dot{m}_{10} \cdot h_{10} - \dot{m}_9 \cdot h_9$
Mass balance for the absorber	$\dot{m}_{13} + \dot{m}_7 = \dot{m}_1 = f \cdot \dot{m}_{13}, \quad f = \frac{y_{10} - x_5}{x_4 - x_5}$
Heat-transfer rate for the rectifier	$\dot{Q}_r = \dot{m}_2 \cdot cp_2 \cdot (t_3 - t_2)$
Specific heat of the NH_3–H_2O solution	$cp_2 = x_2 \cdot cp_{NH3} + (1 - x_2) \cdot cp_{H2O}$
Enthalpy at state 6	$h_6 = h_{NH_3H_2O}(t_6, x_6, Q_6 = 0)$
Energy balance for the SHX	$\dot{m}_3 \cdot h_3 + \dot{m}_5 \cdot h_5 - \dot{m}_4 \cdot h_4 - \dot{m}_6 \cdot h_6 = 0$
Heat-transfer rate for the remaining absorption refrigeration components	$\dot{Q}_a = \dot{m}_{13} \cdot h_{13} + \dot{m}_7 \cdot h_7 - \dot{m}_1 \cdot h_1$ $\dot{Q}_c = \dot{m}_{10} \cdot (h_{10} - h_{11})$ $\dot{Q}_e = \dot{m}_{12} \cdot (h_{13} - h_{12})$ $\dot{Q}_{SHX} = \dot{m}_3 \cdot (h_4 - h_3)$
Solution pump work	$\dot{W}_p = (p_2 - p_1) \cdot v_1 \cdot \frac{\dot{m}_1}{\eta_p} \cdot 1000$ $v_1 = v_{NH_3H_2O}(t_1, p_1, Q_1 = 0)$
COP of the system	$COP = \frac{\dot{Q}_e}{\dot{Q}_g + \dot{W}_p}$
Efficiency of the CCP and CCHP	$\eta_{CCP} = \frac{\dot{Q}_e + N_{el}}{\dot{m}_{fuel} \cdot LHV}$ and $\eta_{CCHP} = \frac{\dot{Q}_e + N_{el} + \dot{Q}_{tank}}{\dot{m}_{fuel} \cdot LHV}$
Model constrains	
Restriction in a mass fraction	$\Delta_X = X_1 - X_5 > 0$

Table 4: Process conditions as input to the AR systems

Parameter	LiBr–H_2O		NH3–H_2O	
	Symbol	Value	Symbol	Value
Absorber temperature (°C)	t_1	35.5	t_1	40
Condenser temperature (°C)	t_8	39.8	t_{11}	40
Inlet cooling temperature of absorber and condenser	$t_{11} = t_{15}$	25	$t_{16} = t_{20}$	25
Evaporator temperature	t_{10}	8.6	t_{10}	-10
Generator-outlet temperature	t_4	84.8	t_5	124
Mass flow rate of weak solution (kg/s)	m_1	–	m_1	1
Effectiveness of generator and solution heat exchanger	$\varepsilon_{SHX} = \varepsilon_{GHX}$	0.707	$\varepsilon_{SHX} = \varepsilon_{GHX}$	0.8
Effectiveness of evaporator and gas–water heat exchanger	ε_{EHX}	0.64	ε_{EHX}	0.64
Evaporator cooling load (kW)	Q_e	201.29	–	–
Difference in mass fraction between strong and weak solutions	–	–	Δ_X	0.1
Vapour quality at the evaporator outlet	Q_{13}	–	Q_{13}	0.975
Temperature approach for generator	$\Delta_{app,g}$	10	$\Delta_{app,g}$	10
Temperature difference for condenser and absorber	$\Delta T_c = \Delta T_a$	5	$\Delta T_c = \Delta T_a$	5
Water-storage-tank inlet/outlet temperature	$t_{water,in}/t_{water,out}$	40/90	$t_{water,in}/t_{water,out}$	40/90
Pump efficiency	η_p	0.95	η_p	0.95

2 Results and discussion

The SOFC model was used to generate 15 cases by varying the fuel utilization between 75% and 95% and the current density between 100 and 300 mA/cm² (Table 6). The output from the SOFC model was used as an input to the considered AR systems. The combined results were used to examine the COP of cold production and CCHP efficiency of the integrated system. For each of the considered AR systems,

Table 5: Validation of LiBr–H_2O and NH_3–H_2O models

Parameter	LiBr–H_2O			NH3–H_2O		
	This work	Rubio-Maya et al. [30]	ARD%	This work	Keith et al. [31]	ARD%
High-side pressure (MPa)	0.007030	0.00735	4.35	1.556	1.555	0.06
Low-side pressure (MPa)	0.001118	0.00112	0.18	0.2906	0.288	0.90
Rich-solution mass flow rate (kg/s)	0.696600	0.65900	5.71	1	1	0.00
Weak-solution mass flow rate (kg/s)	0.782300	0.74500	5.01	0.8574	0.858	0.07
Refrigerant mass flow rate (kg/s)	0.085660	0.08600	0.40	0.1529	0.153	0.07
LiBr or NH_3 concentration in strong solution (–)	0.599200	0.59960	0.07	0.3986	0.3971	0.38
LiBr or NH_3 concentration in weak solution (–)	0.533600	0.53070	0.55	0.2986	0.2971	0.50
Absorber heat-transfer rate (kW)	247.9000	247.470	0.17	272.8	275.8	1.09
Condenser heat-transfer rate (kW)	211.2000	213.370	1.02	159.3	157.2	1.34
Evaporator heat-transfer rate (kW)	201.3000	201.300	0.00	147.5	147.2	0.20
Generator heat-transfer rate (kW)	256.4000	259.550	1.21	286.9	284.2	0.95
Coefficient of performance (–)	0.785200	0.77550	1.25	0.4473	0.445	0.52
Rectifier heat-transfer rate (kW)	–	–		42.78	45	4.93
SHX heat-transfer rate (kW)	–	–		258.3	256	0.90

the most optimal operating conditions of the SOFC, which yield the highest CCHP efficiency, have been determined. The results for the most favourable operating conditions of the AR systems were used to perform the sensitivity analysis to evaluate the effect of the operating conditions on the AR-system performance. Different cooling applications were also investigated to determine the required evaporator temperature and corresponding COP for each cooling and refrigeration application for both considered AR systems.

2.1 SOFC performance

The performance of the SOFC under varying operating conditions is presented in Table 6, including the thermodynamic performance and the characteristics of the SOFC exhaust gas (state 15 in **Fig. 1**). This analysis revealed that Case 6, in which the SOFC operated with a fuel-utilization factor of 0.85 and a current density of 100 mA/cm^2, was characterized with the highest net power output and the electrical efficiency of 123.66 kW and 57.5%, respectively. In Cases 6–15, an increase in the current density resulted in a reduction in the net power output and, subsequently, the electrical efficiency of the SOFC. Conversely, an increase in the fuel-utilization factor at constant current density led to an increase in the SOFC power output and, subsequently, electrical efficiency. Because fuel utilization of >85% can be difficult to achieve, Case 6 was considered in further analysis. It also needs to be emphasized that the lower the current density, the higher the SOFC area required. This will subsequently lead to a higher capital cost of the SOFC. The economic assessment is out of the scope of this work. Moreover, determination of the optimum operating conditions for the combined SOFC–AR system needs to consider the CCHP performance.

2.2 Integrated-system performance

As the models developed in this work were shown to accurately represent both LiBr–H_2O and NH_3–H_2O systems, these were used to assess the performance of the AR integrated with the SOFC and HWST.

Table 7 presents the performance of the integrated LiBr–H_2O system. The best operating conditions for the AR cycle and the integrated system have been observed in Case 6 that is characterized by a COP of 0.8058 and CCHP efficiency of 85.2%. It can be observed that Case 1, for which the temperature and mass flow rate of the exhaust gas from the SOFC were higher than those in Case 6, achieved similar COP and CCHP efficiency. This indicates that the performance of the considered integrated system is not significantly influenced by a SOFC exhaust-gas temperature >150°C. Conversely, if the temperature of the SOFC exhaust gas fell to <150°C, the performance of the AR cycle and the integrated system was substantially affected. This can be clearly seen in Case 5 in which the exhaust-gas temperature is 123.3°C and the corresponding COP and CCHP efficiency are 0.3869 and 72.2%, respectively. Moreover, the minimum generator-outlet temperature for the integrated LiBr–H_2O system is 71°C. This

Table 6: SOFC simulation results for selected output parameters

Parameter/case	1	2	3	4	5	6	7	8	9	10	11	12	13	14	15
Variable parameters															
Fuel-utilization factor (–)	0.75	0.8	0.85	0.9	0.95	0.85	0.85	0.85	0.85	0.85	0.85	0.85	0.85	0.85	0.85
Current density (mA/cm^2)	180	180	180	180	180	100	120	140	160	200	220	240	260	280	300
Results for selected SOFC output parameters															
Temperature (°C)	538.5	378.5	284.6	224.1	182.5	427.1	372.4	333.9	306.3	267.9	254.1	242.8	233.3	225.3	218.3
Pressure (bar)	1.08	1.08	1.08	1.08	1.08	1.08	1.08	1.08	1.08	1.08	1.08	1.08	1.08	1.08	1.08
Mass flow rate (kg/s)	0.18	0.26	0.34	0.43	0.53	0.17	0.21	0.26	0.30	0.39	0.43	0.48	0.53	0.57	0.62
CO_2 mass fraction (–)	0.065	0.046	0.035	0.028	0.023	0.070	0.056	0.047	0.040	0.031	0.028	0.025	0.023	0.021	0.019
H_2O mass fraction (–)	0.052	0.036	0.028	0.022	0.018	0.056	0.045	0.037	0.032	0.024	0.022	0.020	0.018	0.017	0.015
O_2 mass fraction (–)	0.133	0.163	0.180	0.190	0.198	0.125	0.147	0.161	0.172	0.186	0.191	0.195	0.198	0.201	0.203
N_2 mass fraction (–)	0.750	0.755	0.758	0.760	0.761	0.749	0.753	0.755	0.757	0.759	0.760	0.761	0.761	0.762	0.762
Specific heat (kJ/kg°C)	1.17	1.11	1.08	1.06	1.05	1.15	1.12	1.10	1.09	1.07	1.07	1.06	1.06	1.05	1.05
Net electrical efficiency (%)	45.5	47.7	49.7	51.4	52.8	57.5	55.6	53.7	51.7	47.7	45.6	43.5	41.5	39.3	37.2
Net power output (kW)	97.68	102.47	106.76	110.49	113.47	123.66	119.54	115.33	111.07	102.41	98.01	93.57	89.09	84.55	79.74

Table 7: Performance of the integrated LiBr–H_2O system

Parameters	Case	t_{17} (°C)	t_4 (°C)	N_{el} (kW)	$\dot{Q}_{HWST}$ (kW)	$\dot{Q}_g$ (kW)	$\dot{Q}_e$(kW)	COP (−)	η_{CCP} (−)	η_{CCHP} (−)
Most optimal	6	211.4	89.1	123.66	42.18	21.95	17.69	0.8058	0.6565	0.8524
Optimal	1	251.5	97.1	97.68	60.45	30.41	24.38	0.8017	0.5669	0.8476
	7	191.7	85.1	119.54	42.51	22.71	18.29	0.8056	0.6401	0.8375
	8	177.8	82.4	115.33	44.65	24.44	19.63	0.8031	0.6268	0.8341
	2	193.8	85.6	102.47	53.28	28.37	22.86	0.8057	0.582	0.8295
	9	167.9	80.4	111.07	45.26	25.34	20.25	0.7989	0.6099	0.8201
	3	160	78.8	106.76	45.73	26.16	20.75	0.7932	0.5922	0.8046
	10	154	77.6	102.41	47.51	27.73	21.80	0.7863	0.5769	0.7975
Average	11	149.1	76.6	98.01	48.33	28.75	22.36	0.7780	0.559	0.7835
	4	138.3	74.4	110.49	39.12	24.54	18.22	0.7424	0.5977	0.7794
	12	145	75.8	93.57	49.75	30.13	23.15	0.7683	0.5421	0.7732
	13	141.6	75.1	89.09	51.54	31.74	24.04	0.7573	0.5254	0.7648
Poor	14	138.7	74.5	84.55	51.81	32.42	24.14	0.7446	0.5048	0.7454
	15	136.2	74.0	79.94	53.47	33.96	24.80	0.7301	0.4864	0.7347
Marginal	5	123.3	71.5	113.47	32.96	23.3	9.08	0.3896	0.5691	0.7222

means that, in Case 5, the AR cycle operates under marginal conditions with a generator-outlet temperature (t_4) of 71.5°C. Since Case 6 achieved the most optimal operating conditions among the considered cases, it will be used in further analysis of the integrated LiBr–H_2O system.

The performance of the integrated NH_3–H_2O system is presented in Table 8. The best performance of the NH_3–H_2O system has been observed in Case 1, for which the COP was 0.6571. Yet, considering the combined heat and power (CHP) efficiency of the integrated NH_3–H_2O system, which comprises the SOFC and the GWHX, Case 6 has been shown to yield the best performance, with a COP equal to 0.6490 and CCHP efficiency of 83.6%. Therefore, Case 6 is considered in further analysis of the integrated NH_3–H_2O system. Similarly to the integrated LiBr–H_2O system, if the temperature of the SOFC exhaust gas fell to <150°C, the performance of the NH_3–H_2O cycle and the integrated system was substantially affected. In Case 5, in which the exhaust-gas temperature was 123.3°C, the COP and CCHP efficiency of the integrated NH_3–H_2O system were only 0.1466 and 69.6%, respectively. It can be noted that the same operating conditions of the SOFC resulted in the most optimum case for both considered AR systems, enabling a direct comparison.

2.3 Effect of absorber and condenser temperature on integrated-system performance

In the considered AR cycles, heat rejection takes place in the absorber and the condenser, with both units being cooled using ambient air. The effect of the operating temperature of these unit operations on the performance of the AR cycles and the integrated systems was assessed by varying the initial value (35.5°C for the absorber and 39.8°C for the condenser) by ±15%. The effects of the absorber temperature on the COP and heat-transfer rate in the evaporator and the generator for the integrated LiBr–H_2O and NH_3–H_2O systems are shown in **Fig. 4**. In both AR cycles, an increase in the absorber temperature resulted in a decrease in the COP, leading to subsequent reductions in the CCHP efficiency and the heat-transfer rates in the evaporator and the generator. Importantly, for each 5% variation in the absorber temperature, the COP changed by ±0.7% and ±1.1% for the LiBr–H_2O system and the NH_3–H_2O system, respectively. In the NH_3–H_2O system, a sharp drop in the COP was observed when the absorber temperature was equal to the condenser temperature (39.8°C). It also needs to be highlighted that the CCHP efficiency was not as significantly influenced by the absorber temperature as was the CHP efficiency. Yet, operation at lower absorber temperatures, which depend on the inlet temperature of the cooling air, would result in maximizing the overall system efficiency.

Furthermore, the effect of the absorber temperature on the concentration of weak and strong solutions in both integrated systems is presented in **Fig. 5**. For the LiBr–H_2O system (Fig. 5a), an increase in the absorber temperature led to a nearly linear increase in the solution concentration. Consequently, the solution concentrations were shown to

Table 8: Performance of the integrated NH_3–H_2O system

Parameters	Case	t_{14} (°C)	t_5 (°C)	N_{el} (kW)	$\dot{Q}_{HWST}$ (kW)	$\dot{Q}_g$ (kW)	$\dot{Q}_e$ (kW)	COP (−)	η_{CCP} (−)	η_{CCHP} (−)
Most optimal	6	211.4	89.6	123.66	42.18	21.89	14.26	0.6490	0.6405	0.8364
	1	251.5	97.8	97.68	60.45	30.34	20.00	0.6571	0.5465	0.8273
Optimal	7	191.7	85.1	119.54	42.51	22.63	14.53	0.6391	0.6227	0.8201
	8	177.8	82.4	115.33	44.65	24.35	15.35	0.6270	0.6069	0.8142
	2	193.8	85.6	102.47	53.28	28.27	18.19	0.6406	0.5604	0.8079
	9	167.9	80.4	111.07	45.26	25.24	15.58	0.6136	0.5882	0.7984
	3	160	78.8	106.76	45.73	26.04	15.70	0.5984	0.5687	0.7811
	10	154	77.6	102.41	47.51	27.59	16.19	0.5821	0.5508	0.7715
Average	11	149.1	76.6	98.01	48.33	28.59	16.28	0.5642	0.5308	0.7552
	4	138.3	74.4	110.49	39.12	24.39	12.31	0.4984	0.5703	0.7520
	12	145	75.8	93.57	49.75	29.96	16.49	0.5450	0.5112	0.7422
Poor	13	141.6	75.1	89.09	51.54	31.55	16.72	0.5243	0.4914	0.7307
	14	138.7	74.5	84.55	51.81	32.23	16.38	0.5022	0.4688	0.7094
	15	136.2	74.0	79.94	53.47	33.74	16.35	0.4780	0.4472	0.6954
Marginal	5	123.3	71.5	113.47	32.96	23.11	3.493	0.1466	0.5432	0.6962

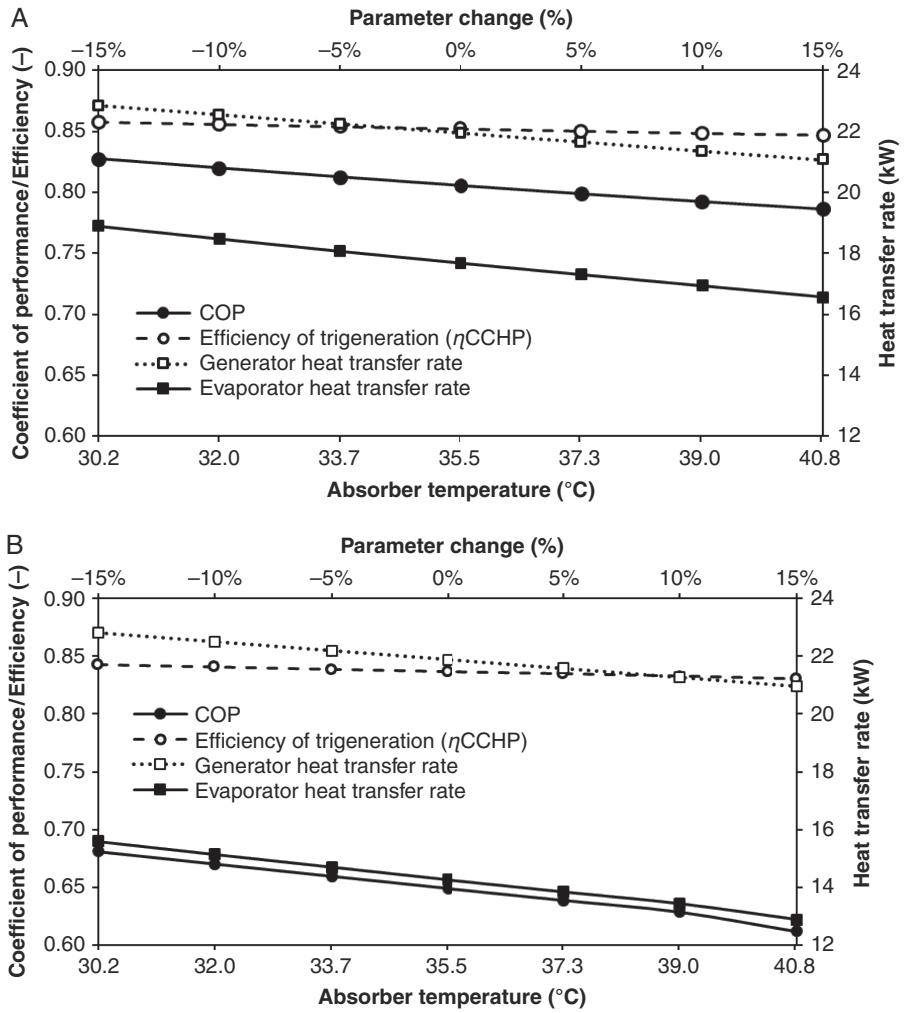

Fig. 4: Absorber-temperature influence on the COP and evaporator/generator heat-transfer rates for (a) the integrated LiBr–H_2O system and (b) the integrated NH_3–H_2O system

gradually approach the crystallization limit. It needs to be emphasized, therefore, that the absorber temperature in the LiBr–H_2O system needs to be carefully monitored to prevent the precipitation of LiBr crystals. The inverse correlation was observed for the NH_3–H_2O system (Fig. 5b), as an increase in the absorber temperature resulted in a reduction in the solution concentration. This can be associated with the increased volatility of NH_3 at higher temperatures.

A variation in the condenser temperature has been shown to influence the performance of both integrated systems in a similar manner as does a variation in the absorber temperature. Namely, for each 5% variation in the condenser temperature, the COP changed by ±0.5% and ±1.2% for the LiBr–H_2O system and the NH_3–H_2O system, respectively, as shown in Fig. 6. However, the opposite trends for the concentration of strong solutions were observed. In the LiBr–H_2O system, a 5% increase in the condenser temperature resulted in a decrease in the LiBr concentration in the strong solution from 0.6183 to 0.6160. Conversely, in the NH_3–H_2O system, a 5% increase in the condenser temperature resulted in an increase in the NH_3 concentration in the strong solution from 0.4579 to 0.4610. A variation in the condenser temperature resulted only in variation in the concentration of the strong solution, as the high pressure in the AR cycle is dictated by the saturation temperature in the condenser that, in turn, influences the rich-solution concentration. It is important to emphasize that, in the NH_3–H_2O system, the COP is more significantly influenced when the temperature of the condenser falls below the temperature of the absorber. The effect of the condenser temperature on the CCHP efficiency is small, as in the case of the absorber temperature. This is because the cooling output in the evaporator accounts for ~10% of the total output of the integrated system (Table 8). Nevertheless, in both integrated systems, the condenser temperature should be maximized to avoid challenges with solution crystallization (LiBr–H_2O) and volatility (NH_3–H_2O).

2.4 Effect of evaporator temperature on integrated-system performance

The evaporator is a key unit operation in the AR system, as it produces the cooling effect. Therefore, a sensitivity analysis was performed to evaluate the effect of the evaporator

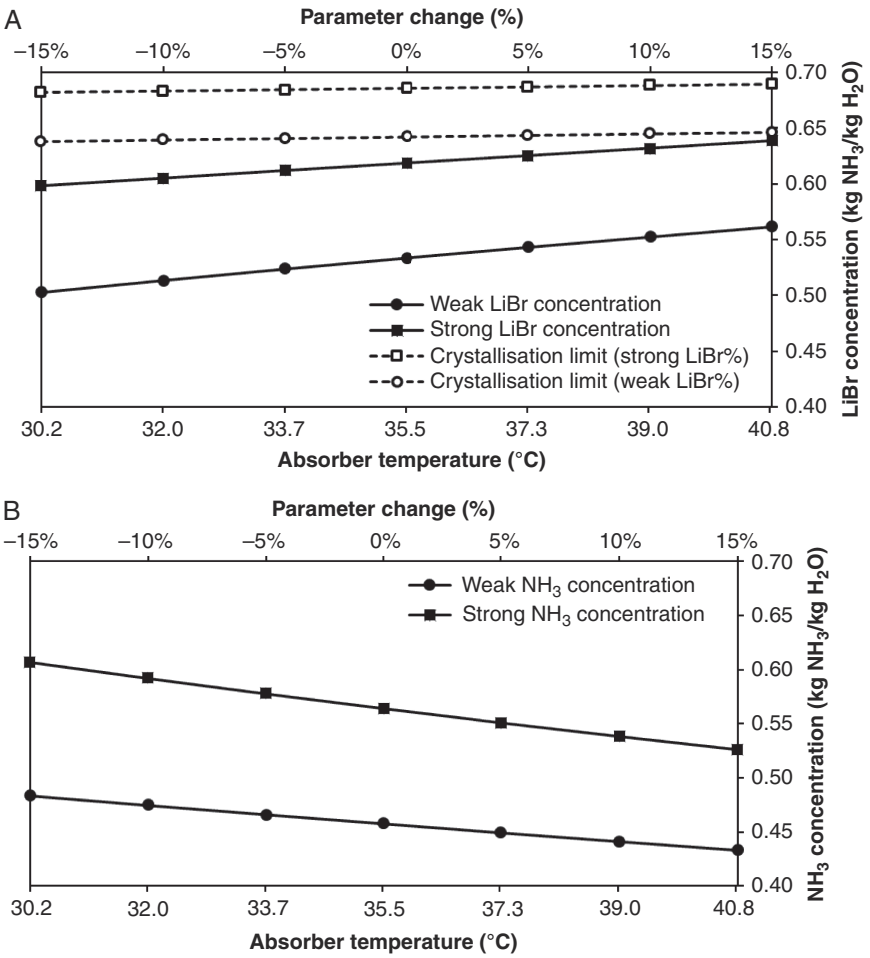

Fig. 5: Absorber-temperature influence on the solution concentration for (a) the integrated LiBr–H_2O system and (b) the integrated NH_3–H_2O system

temperature on the performance of the integrated systems. It is important to emphasize that the evaporator temperature is dictated by the working fluid used in the AR cycle, as, depending on its composition, the minimum evaporator temperature can be determined. For the LiBr–H_2O system, the evaporator temperature needs to be kept >0°C to avoid freezing of the water. Fig. 7 reveals the effect of the evaporator temperature on the performance of the integrated LiBr–H_2O system. It has been shown that a 1°C decrease in the evaporator temperature results in a reduction in the COP and CCHP efficiency of 0.6% and 0.13%, respectively. The decrease in the evaporator temperature also resulted in a subsequent increase in the LiBr concentration in both strong and weak solutions. The substantial concentration difference was shown to be maintained at all evaporator temperatures considered in this sensitivity analysis. This implies that no operational issues should occur in the LiBr–H_2O system.

Conversely to the LiBr–H_2O system, the NH_3–H_2O system can operate with negative evaporator temperatures, providing a cooling effect at substantially lower temperatures. Therefore, the sensitivity analysis was performed by varying the evaporator temperature between –20°C and 20°C. The effect of the evaporator temperature on the performance of the integrated NH_3–H_2O system is shown in Fig. 8. The sensitivity analysis has revealed the near-linear correlation between the evaporator temperature and the performance of the integrated NH_3–H_2O system. A 1°C reduction in the evaporator temperature resulted in a subsequent reduction in the COP and CCHP efficiency by 1.1% and 0.7%, respectively. Such a drop in the performance is sharper than that in the integrated LiBr–H_2O system. Moreover, comparing the results for both considered integrated systems, it can be concluded that the performance of the integrated NH_3–H_2O system (i.e. COP of 0.665 at 10°C) is inferior to the integrated LiBr–H_2O system (i.e. COP of 0.815 at 10°C) for evaporator temperatures >0°C. However, the benefit of the former integrated system is that it can operate with negative evaporator temperatures. Nevertheless, it is important to highlight that the COP of the NH_3–H_2O system decreases from 0.554 at 0°C to 0.341 at –20°C, leading to a subsequent reduction in the CCHP efficiency from 82.3% to 79.6%. Therefore, the selection of the integrated system will depend on the cooling application and the evaporator temperature requirement.

2.5 System-pressure analysis

Each considered AR cycle comprises two pressure levels that are determined from the desired operating conditions

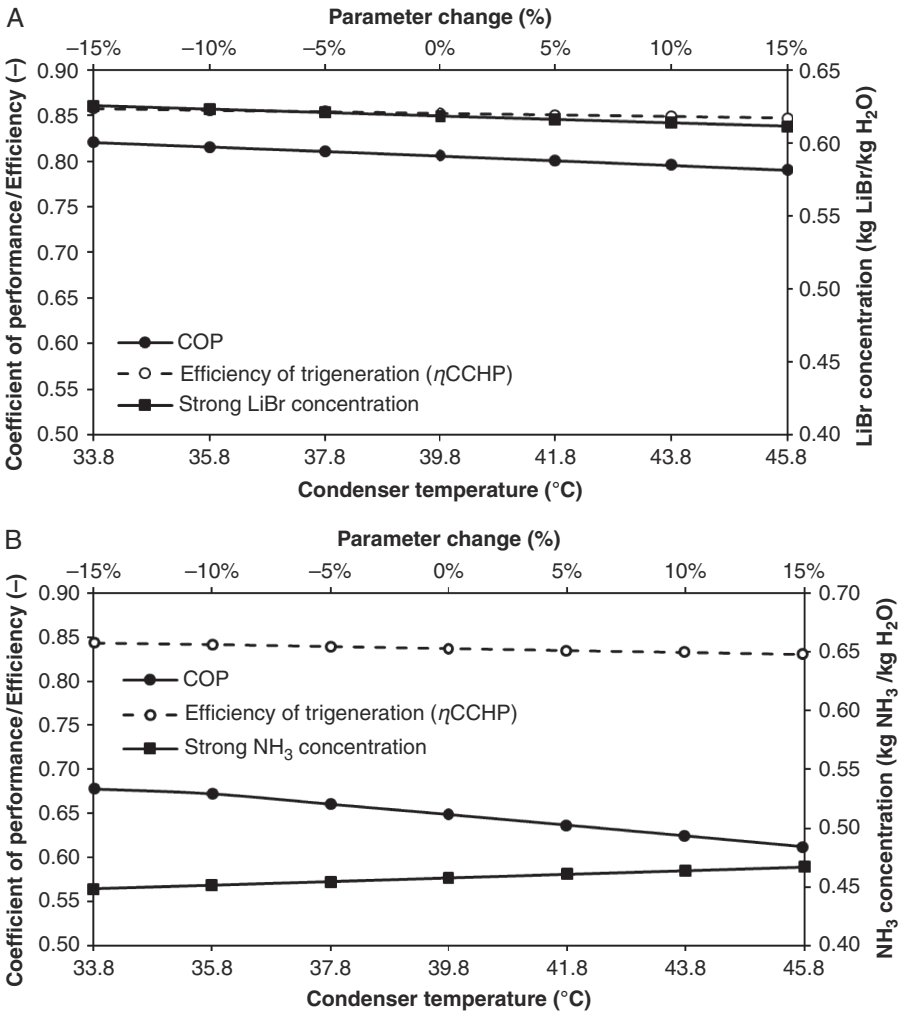

Fig. 6: Condenser-temperature influence on the COP and strong solution concentration for (a) the integrated LiBr–H_2O system and (b) the integrated NH_3–H_2O system

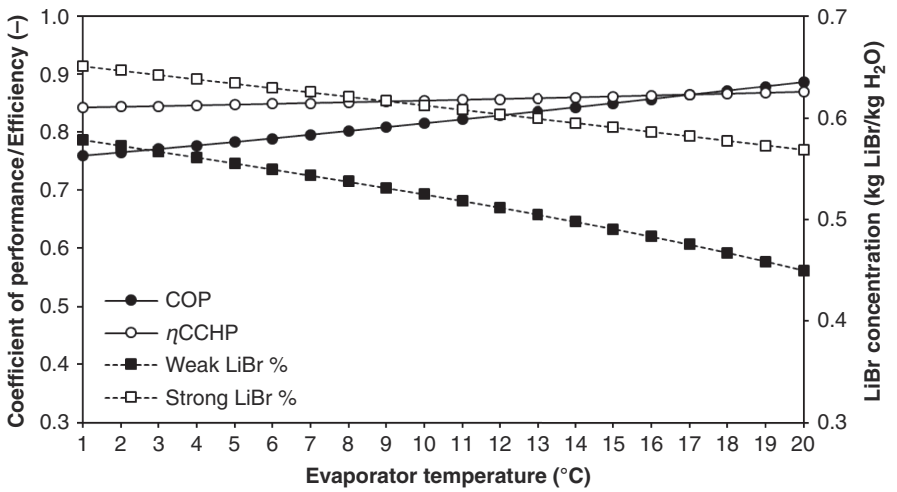

Fig. 7: Effect of the evaporator temperature on the COP and solution concentrations in the integrated LiBr–H_2O system

of the specific AR cycle. Namely, a high-pressure side is determined by the saturation temperature of the condenser and a low-pressure side is influenced by the saturation temperature of the evaporator. A sensitivity analysis has been performed by varying the operating temperature by ±15% to determine the influence of the operating temperature of the condenser and the evaporator on the system pressure. The results for the integrated LiBr–H_2O system

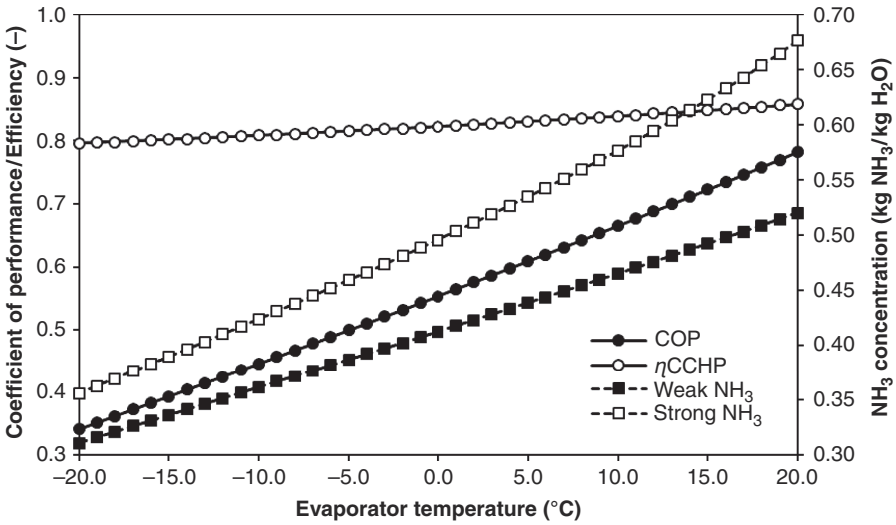

Fig. 8: Effect of the evaporator temperature on the COP and solution concentrations in the integrated NH_3–H_2O system

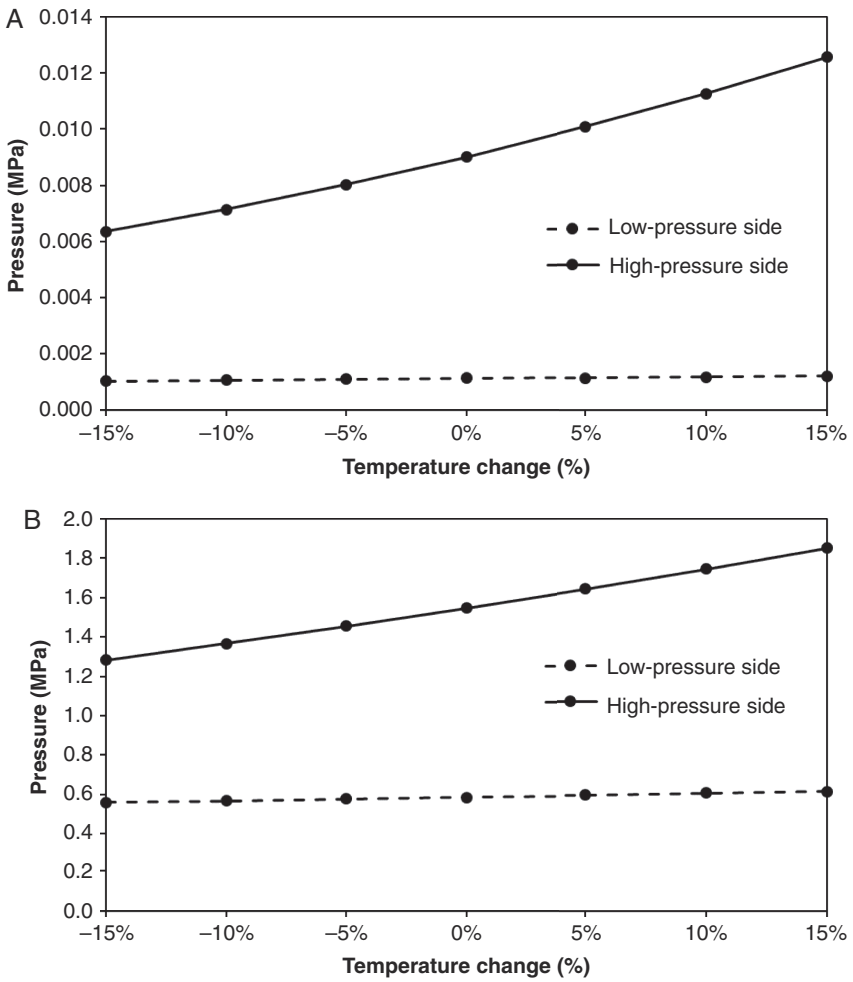

Fig. 9: Pressure levels and its relative change as a function of the evaporator (low-pressure side) and condenser (high-pressure side) temperature in (a) the integrated LiBr–H_2O system and (b) the integrated NH_3–H_2O system

and the integrated NH_3–H_2O system are presented in Fig. 9a and 9b. For both considered systems, a decrease in the evaporator temperature (low-pressure side) resulted in a small reduction in the pressure. Namely, a 5% increase in the evaporator temperature resulted in a pressure increase of 1.5% (the LiBr–H_2O system) and 3% (the NH_3–H_2O system). In contrast, a 5% increase in the condenser temperature (high-pressure side) resulted in a pressure increase of 11% and 6% in the LiBr–H_2O system and the NH_3–H_2O system, respectively. Importantly, the pressure at

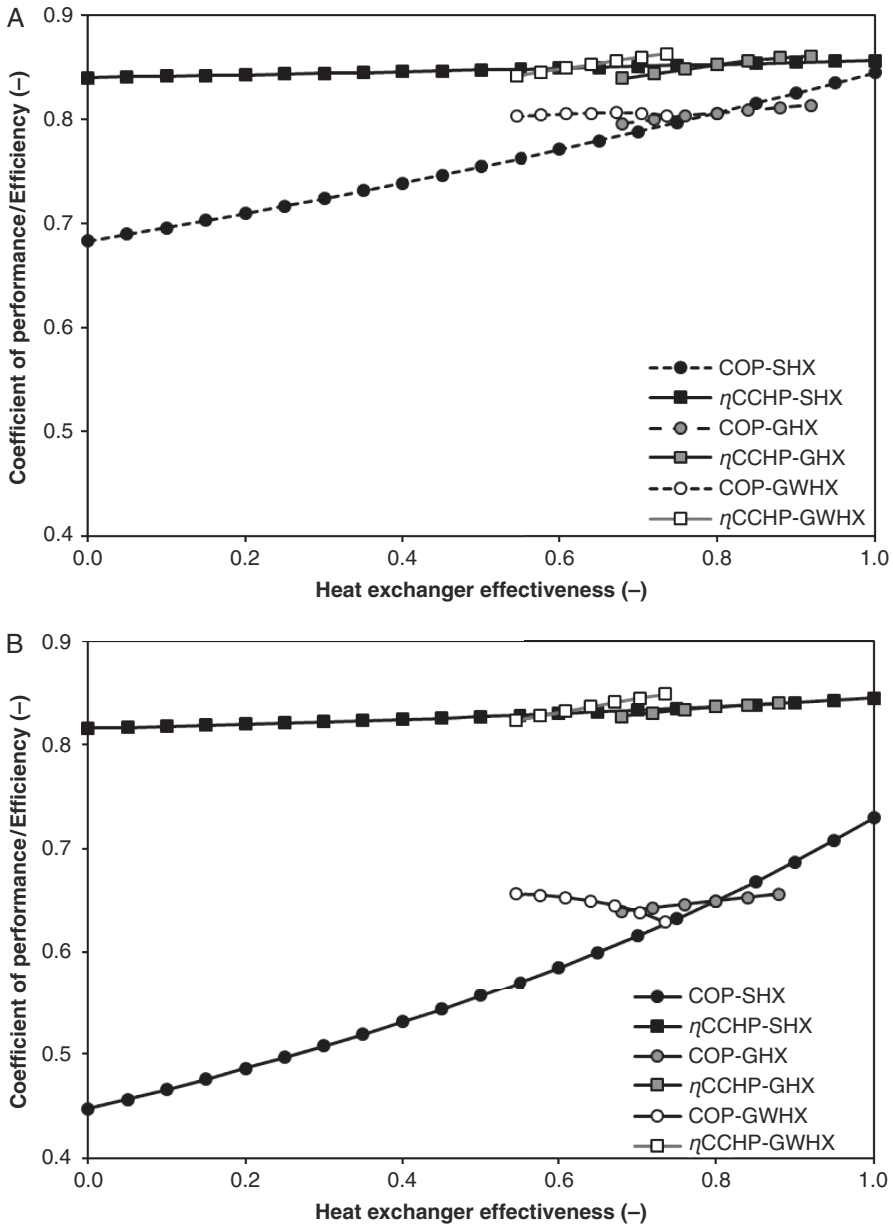

Fig. 10: Effect of the heat-exchanger effectiveness the performance of (a) the integrated LiBr–H_2O system and (b) the integrated NH_3–H_2O system

the low-pressure side of the AR cycles was shown to be more stable within the considered temperature range and would remain constant for a specific cooling application. Conversely, the condenser temperature is influenced by ambient conditions, which could be subject to seasonal variability. This implies the importance of maintaining the condenser temperature at the optimal operating point, especially for the NH_3–H_2O system. This is because excessive pressure can result in system failure and toxic NH_3 release.

2.6 Heat-exchanger analysis

The integrated system comprises three main heat exchangers: (i) the GWHX, which recovers high-grade heat from the SOFC exhaust gas for HWST and conditions the exhaust gas to meet the temperature required by the AR cycle; (ii) the generator heat exchanger (GHX) in which heat from the SOFC exhaust gas is transferred to the AR cycle; and (iii) the solution heat exchanger (SHX), which preheats the weak solution in the LiBr–H_2O system (or strong solution in the NH_3–H_2O system) by exchanging heat with the return solution from the generator. All heat exchangers were modelled using a specified heat-exchanger effectiveness. This parameter has been varied between 0 (no heat transfer) and 1 (maximum heat transfer) for the SHX to assess the influence of the heat-exchanger effectiveness on the integrated-system performance. For the GWHX and GHX, the effectiveness has been varied by ±15% (5% interval) with respect to the initial values in Table 4.

Fig. 10 reveals that that effectiveness of the SHX has a significant impact on the COP, especially in the NH_3–H_2O system. This analysis confirmed the need for the SHX in the AR cycles. The COP in the systems without the SHX was 16% and 31% lower for the LiBr–H_2O system and the

NH_3–H_2O system, respectively, as compared to that in the systems with the SHX at an effectiveness of 0.8. It is important to emphasize that the effectiveness of the SHX had a small influence on the CCHP efficiency. An increase in the SHX effectiveness from 0.8 to 0.95 resulted in a CCHP efficiency increase from 85.2% to 85.3% for the integrated LiBr–H_2O system and 83.7% to 84.3% for the integrated NH_3–H_2O system. Such an increase would not be justified from an economic standpoint, as it would need an increase in the heat-transfer area of the SHX, leading to a higher capital cost. The performance of the integrated systems was shown to be more influenced by the variation in the effectiveness of the GHX and the GWHX. In the latter case, an increase in the effectiveness resulted in a marginal variation in the COP in the LiBr–H_2O system and a decrease in the COP in the NH_3–H_2O system (i.e. a 10% increase in the effectiveness from 0.640 to 0.704 resulted in a COP decrease from 0.649 to 0.638). However, such a change in the GWHX resulted in 0.7–0.8% increase in the CCHP efficiency in both systems, because more heat was transferred from the SOFC exhaust gas to the HWST. In turn, the temperature of the SOFC exhaust gas at the inlet to the generator in the AC cycles was lower, influencing the COP. Furthermore, a nearly linear correlation between the GHX effectiveness and the performance of the integrated system was observed. Namely, a 10% increase in the GHX effectiveness from 0.8 to 0.88 resulted in an increase in the COP of the LiBr–H_2O system and the NH_3–H_2O systems by 0.6% and 0.7%, respectively. In this vein, the CCHP efficiency increased by 0.7% and 0.3%, respectively.

2.7 Industrial applications

A cooling effect produced in the evaporator of the AR cycle is absorbed by an external coil that supplies cold air to the specific cooling or refrigeration application. Each application is characterized not only with different storage-temperature requirements, but also with specific relative humidity associated with the specific product attributes. These parameters determine the temperature difference that is a design parameter for a refrigeration system. It represents the difference between the temperature of return air from the cooling application, which can be assumed to be the same as the storage temperature under steady-state conditions, and the evaporator temperature. To assess the feasibility of using the considered integrated systems, the following product classes have been distinguished based on the evaporator temperature [32, 33]:

- frozen products (–35°C to –7°C);
- low-temperature (LT) products (–6°C to 0°C);
- medium-temperature products (0°C to 7°C); and
- high-temperature (HT) products (7°C to 16°C).

Considering different cooling and refrigeration products, and thus the required evaporator temperature, the performance of the considered integrated systems has been assessed in terms of the COP and evaporator heat-transfer rate. **Fig. 11b** reveals that the NH_3–H_2O system can meet the requirements for all considered cooling and refrigeration applications. However, a substantial drop in the COP has been observed for the very LT applications (i.e. frozen products). Application of the integrated LiBr–H_2O system (**Fig. 11a**) has been restricted to HT and MT products to avoid freezing of the refrigerant to <0°C. Given its higher COP, the integrated LiBr–H_2O system would be preferred over the integrated NH_3–H_2O system for all cooling applications that require an evaporator temperature of >0°C. The latter system, however, will be preferred for applications that require an evaporator temperature of <0°C. However, with a very low heat-transfer rate in the evaporator operating at very low temperatures, this system can be limited to refrigeration applications with a small capacity (i.e. defined by the total volume occupied by the products) such as refrigeration trucks or small-scale cold rooms. The large-scale application may be limited by the capacity and capital cost of the SOFC, and therefore further economic evaluation is required.

3 Conclusion

This study aimed to assess the performance of AR systems integrated with the HWST and the SOFC. The thermodynamic models for the LiBr–H_2O and NH_3–H_2O systems have been developed in EES and integrated with the SOFC model developed in Aspen Plus®. The most optimal operating conditions of the integrated system resulted in the COP and the CCHP efficiency of 0.806 and 85.2% for the LiBr–H_2O system and 0.649 and 83.6% for the NH_3–H_2O system, respectively. Under the optimal operating conditions, a net electrical efficiency of 57.5% and a net power output of 123.66 kW from the SOFC has been obtained. The most optimal case has been used to carry out a sensitivity study. The outputs of the sensitivity study have revealed that:

- increasing the heat-rejection temperature led to a lower COP in both AR systems. A drop equal to ~1% was observed for each 5% temperature growth in both AR models;
- in the LiBr–H_2O system, attention must be paid to the absorber and generator temperatures to avoid the precipitation of LiBr crystals that can occur at high operating temperatures;
- the evaporator temperature showed an almost linear correlation with the COP of the AR systems. A decrease of 0.6% and 1.1% per 1°C temperature drop was observed for the LiBr–H_2O and NH_3–H_2O systems, respectively;
- the pressures within a system are determined by the evaporator and condenser temperatures. The high-pressure side was shown to be more sensitive to the temperature changes than the low-pressure side. Approximately ±11% pressure change for the LiBr–H_2O system and ±6% in the NH_3–H_2O system for each 5% temperature variation was observed. This indicated the need for monitoring of the condenser temperature;

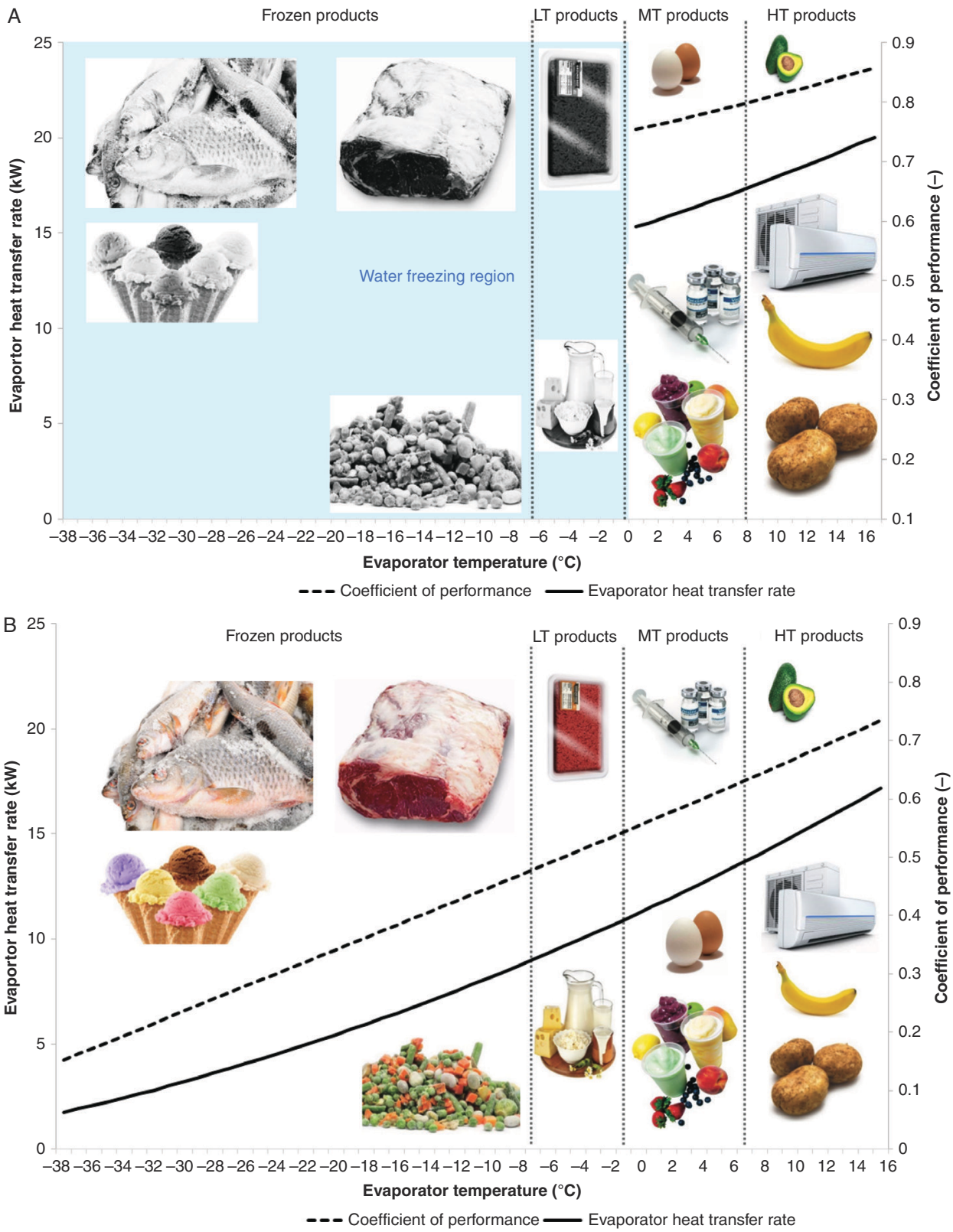

Fig. 11: The COP and evaporator heat-transfer rate for different cooling and refrigeration applications of (a) the integrated LiBr–H_2O system and (b) the integrated NH_3–H_2O system

- the heat-exchanger effectiveness for the main heat exchangers of the integrated system has been analysed. The effectiveness of the SHX had the largest influence on the AR-cycle performance. A comparison has been made between the COP with and without the SHX and a drop in the COP of 16% for the LiBr–H_2O system and 31% for the NH_3–H_2O system has been observed, implying the importance of the SHX; and

- the application of the integrated LiBr–H_2O system is restricted to applications that require cooling to >0°C.

Overall, this study has revealed that the integrated LiBr–H_2O system will be characterized by better performance than that of the integrated NH_3–H_2O system for all cooling applications that require an evaporator temperature of >0°C. For refrigeration applications that require cooling to <0°C, the integrated NH_3–H_2O system will be preferred. Further work should be carried out to compare the economic performance of the considered systems and to consider AR systems using alternative working fluids.

Supplementary data

Supplementary data is available at *Clean Energy* online.

Conflict of Interest

None declared.

References

[1] Pardo N, Vatopoulos K, Krook-Riekkola A, *et al*. *Heat and Cooling Demand and Market Perspective*. Petten: Joint Research Centre, Institute for Energy and Transport, 2012.

[2] Ranjbar F, Chitsaz A, Mahmoudi SMS, *et al*. Energy and exergy assessments of a novel trigeneration system based on a solid oxide fuel cell. *Energ Convers Manage* 2014, 87:318–27.

[3] Zabihian F, Fung AS. Performance analysis of hybrid solid oxide fuel cell and gas turbine cycle: application of alternative fuels. *Energ Convers Manage* 2013, 76:571–80.

[4] Akkaya AV, Sahin B. A study on performance of solid oxide fuel cell-organic Rankine cycle combined system. *Int J Energ Res* 2009, 33:553–64.

[5] Vera D, Jurado F, Carpio J. Study of a downdraft gasifier and externally fired gas turbine for olive industry wastes. *Fuel Process Technol* 2011, 92:1970–9.

[6] Vera D, Jurado F, Carpio J, *et al*. Biomass gasification coupled to an EFGT-ORC combined system to maximize the electrical energy generation: a case applied to the olive oil industry. *Energy* 2018, 144:41–53.

[7] El-Sattar HA, Kamel S, Vera D, *et al*. Tri-generation biomass system based on externally fired gas turbine, organic Rankine cycle and absorption chiller. *J Clean Prod* 2020, 260:121068.

[8] El-Sattar HA, Kamel S, Jurado F. Fixed bed gasification of corn stover biomass fuel: Egypt as a case study. *Biofuel Bioprod Biorefin* 2020, 14:7–19.

[9] Ozcan H, Dincer I. Performance evaluation of an SOFC based trigeneration system using various gaseous fuels from biomass gasification. *Int J Hydrogen Energ* 2015, 40:7798–807.

[10] Kendall K, Kendall M. *High-temperature Solid Oxide Fuel Cells for the 21st Century*, 2nd edn. London: Elsevier, 2015.

[11] Al-Sulaiman FA, Dincer I, Hamdullahpur F. Exergy analysis of an integrated solid oxide fuel cell and organic Rankine cycle for cooling, heating and power production. *J Power Sources* 2010, 195:2346–54.

[12] Yu Z, Han J, Cao X. Investigation on performance of an integrated solid oxide fuel cell and absorption chiller trigeneration system. *Int J Hydrogen Energ* 2011, 36:12561–73.

[13] Zhao H, Jiang T, Hou H. Performance analysis of the SOFC–CCHP system based on H_2O/Li–Br absorption refrigeration cycle fueled by coke oven gas. *Energy* 2015, 91:983–93.

[14] Venkataraman V, Pacek AW, Steinberger-Wilckens R. Coupling of a solid oxide fuel cell auxiliary power unit with a vapour absorption refrigeration system for refrigerated truck application. *Fuel Cells* 2016, 16:273–93.

[15] Elmer T, Woralla M, Wua S, Riffat S. Assessment of a novel solid oxide fuel cell tri-generation system for building applications. *Energ Convers Manage* 2016, 124:29–41.

[16] Hou Q, Zhao H, Yang X. Thermodynamic performance study of the integrated MR-SOFC-CCHP system. *Energy* 2018, 150:434–50.

[17] Hanak DP, Jenkins BG, Kruger T, *et al*. High-efficiency negative-carbon emission power generation from integrated solid-oxide fuel cell and calciner. *Appl Energ* 2017, 205:1189–201.

[18] Zhang W, Croiset E, Douglas PL, *et al*. Simulation of a tubular solid oxide fuel cell stack using AspenPlusTM unit operation models. *Energ Convers Manage* 2005, 46:181–96.

[19] Doherty W, Reynolds A, Kennedy D. Computer simulation of a biomass gasification-solid oxide fuel cell power system using Aspen Plus. *Energy* 2010, 35:4545–55.

[20] Song TW, Sohn JL, Kim JH, *et al*. Performance analysis of a tubular solid oxide fuel cell/micro gas turbine hybrid power system based on a quasi-two dimensional model. *J Power Sources* 2005, 142:30–42.

[21] Achenbach E. Three-dimensional and time-dependent simulation of a planar solid oxide fuel cell stack. *J Power Sources* 1994, 49:333–48.

[22] Chan SH, Khor KA, Xia ZT. A complete polarization model of a solid oxide fuel cell and its sensitivity to the change of cell component thickness. *J Power Sources* 2001, 93:130–40.

[23] Bessette NF, Wepfer WJ, Winnick J. A mathematical model of a solid oxide fuel cell. *J Electrochem Soc* 1995, 142:3792–800.

[24] Veyo S, Forbes C. Demonstrations based on Westinghouse's prototype commercial. In: Stevens P (ed.). *Proceedings of the Third European Solid Oxide Fuel Cell Forum*, Nantes, France, 2–5 July 1998, 79–86. European Fuel Cell Forum.

[25] Veyo S. The Westinghouse solid oxide fuel cell program—a status report. In: Chetty, PRK (ed.). *Proceedings of the 31st Intersociety Energy Conversion Engineering Conference*, Washington, DC., 11–16, August 1996, 1138–43. Institute of Electrical and Electronic Engineers.

[26] Veyo S, Lundberg W. Solid oxide fuel cell power system cycles. In: *ASME 1999 International Gas Turbine and Aeroengine Congress and Exhibition*, Indianapolis, IN., 7–10 June 1999, V002T02A058. American Society of Mechanical Engineers.

[27] Habibollahzade A, Gholamian E, Behzadi A. Multi-objective optimization and comparative performance analysis of hybrid biomass-based solid oxide fuel cell/solid oxide electrolyzer cell/gas turbine using different gasification agents. *Appl Energ* 2019, 233–234:985–1002.

[28] Hauck M, Herrmann S, Spliethoff H. Simulation of a reversible SOFC with Aspen Plus. *Int J Hydrogen Energ* 2017, 42:10329–40.

[29] Gilani SIUH, Ahmed MSMS. Solution crystallization detection for double-effect LiBr-H_2O steam absorption chiller. *Energy Procedia* 2015, 75:1522–8.

[30] Rubio-Maya C, Pacheco-Ibarra JJ, Belman-Flores JM, *et al*. NLP model of a LiBr-H_2O absorption refrigeration system for the minimization of the annual operating cost. *Appl Therm Eng* 2012, 37:10–8.

[31] Herold KE, Radermacher R, Klein SA. *Absorption Chillers and Heat Pumps*, 1st edn. Boca Raton, London, New York, NY and Washington, DC: CRC Press, 1996.

[32] ASHRAE. *ASHRAE Handbook—Refrigeration: Commodity Storage Requirements*. Atlanta, GA: American Society of Heating and Air-Conditioning Engineers, 2014.

[33] HRP. *Commercial Refrigeration Cooling and Freezing Load Calculations and Reference Guide*. Stone Mountain, GA: Heatcraft Refrigeration Products LLC, 2008.

Nomenclature

Symbols	
$\dot{m}$	Mass flow rate (kg/s)
$\dot{n}$	Molar flow rate (kmol/s)
$\dot{Q}$	Heat-transfer rate (kW)
$\dot{W}$	Work input to the pump (kW)
$\dot{C}$	Heat capacity (W/°C)
f	Circulation ratio
F	Faraday constant (C/kmol)
h	Specific enthalpy (kJ/kg)
I	Current density (mA/cm^2)
N_{el}	Electricity production from SOFC (kW)
p	Pressure (MPa)
Q	Vapour quality
S/C	Steam/carbon ratio
T	Temperature (K)
t	Temperature (°C)
U	Cell voltage (V)
u_f	Fuel-utilization factor
v	Specific volume (m^3/kg)
X	Composition of LiBr–H_2O/NH_3–H_2O solution
x	Mass fraction of liquid NH_3 solution
y	Mass fraction of vapour NH_3 solution
ε	Heat-transfer/heat-exchanger effectiveness
η	Efficiency
ρ	Density (kg/m^3)
ω	Mass fraction of NH_3 in liquid or vapour state

Integration of solid-oxide fuel cells and absorption refrigeration for efficient combined cooling, heat and power production

Matuszny, Krzysztof

2020-12-22

Matuszny K, Borhani TN, Nabavi SA, Hanak DP. (2020) Integration of solid-oxide fuel cells and absorption refrigeration for efficient combined cooling, heat and power production. Clean Energy, Volume 4, Issue 4, 2020, pp. 328-348

https://doi.org/10.1093/ce/zkaa019